Applied Physics A (2022) 128:287
https://doi.org/10.1007/s00339-022-05417-z

Applied Physics A
Materials Science & Processing

Synthesis of diamond crystal growth on tungsten carbide inserts by HFCVD using various seeding powders

Ayashkanta Jena[1] · Sisira Kanta Pattnaik[1] · Binod Bihari Palei[2] · Saroj Kumar Sarangi[1]

Received: 3 January 2022 / Accepted: 16 February 2022 / Published online: 13 March 2022

Abstract

The hot filament chemical vapor deposition (HFCVD) process is used to synthesize diamond crystals on cemented carbide (WC–Co) SPUN inserts. Diamond (Dia.), carbon (GC-glassy spherical form), iridium (Ir), molybdenum (Mo), palladium (Pd), platinum (Pt), tungsten (W), and tantalum (Ta) powders were used as seeding materials for crystal growth. Scanning electron microscopy (SEM) data revealed the development of a few diamond crystals in platinum, iridium, and tungsten powders. The seeding with carbon, tantalum, and diamond powders formed clustered microcrystalline diamond (MCD) crystals, although other powders produced discrete crystals. Tantalum and diamond-seeded powders produced the most significant number and size of crystals. According to micro-Raman spectroscopy (μ-RS), tantalum powder had the lowest I_D/I_G ratio and the most excellent sp^3 bonding. X-ray diffraction (XRD) revealed the maximum diamond intensity in the (111) plane. According to atomic force microscopy (AFM), diamond and molybdenum powders had the largest grains, whereas tantalum powder had the smallest root mean square roughness value with a homogeneous grain distribution. The Vickers microhardness (VHN) test confirmed the highest hardness value for diamond and tantalum seeded powder coatings with the least amount of radial cracking. Field emission scanning electron microscopy (FESEM) revealed that both powders had higher film thickness values.

Keywords SPUN cemented carbide · HFCVD · Surface characterization · Grain size · Microhardness · Cutting tools

1 Introduction

Electro-mechanical applications are found for low-pressure diamond synthesis, which deposits thin diamond films [1]. However, several factors determine smooth diamond growth. The mobility of carbon (C) atoms influences film adhesion and coating properties during diamond deposition. The chemical reaction of C with cemented carbides promotes C precipitation during diamond deposition, which prevents diamond–carbide bonding at the interface. Subsequently, the formation of graphite (the thermodynamically stable carbon phase) hampers the nucleation process [2]. Therefore, the use of transitional metal (TM) powders ensures that transitions from graphite to diamond phases are smooth. The ease of carbide formation at the substrate surface with TM powders determines the development of an even diamond film. Metal carbides act as a diffusion barrier in the substrate, preventing carbon diffusion and simplifying the nucleation process. Diamond nucleation and growth kinetics increase as the density of TM powders embedded in the substrate surface increases. The clustered C atoms in the subsurface region of TM powders and the type of TM seed powders used influence the nucleation process. Seeding with W, Mo, and Nb powder on a silicon (Si) substrate, the carbides form rapidly, along with the film's highest nucleation density and columnar structure [3]. Itoh et al. demonstrated that a small-sized seeding powder would result in higher nucleation density due to the more significant number of grains than a larger-sized powder for a given weight percent of powder. Therefore, the grain's collision frequency increases when subjected to an ultrasonic reactor. As a result, the number of nucleating sites increases. Chakk et al. found a linear increase in nucleation density with increasing seeding powder size. However, Baudrillart et al. and Verga et al. found results consistent with Itoh et al. Furthermore, Verga et al.

✉ Saroj Kumar Sarangi
sarojsarangi@gmail.com

[1] Department of Mechanical Engineering, Veer Surendra Sai University of Technology, Burla 768018, Odisha, India

[2] CSIR-Institute of Minerals and Materials Technology, Bhubaneswar 751013, Odisha, India

reported that the nucleation density is affected not only by the powder size but also by the composition, morphology, and weight percentage of the powder [4–7].

Seeding and nucleation are typically performed after mechanical and/or chemical treatment in an ultrasonic bath. A suitable chemical pre-treatment optimally reduces the cobalt (Co) content in the cemented carbide substrate (etching) while increasing diamond nucleation. On the other hand, complete Co removal will reduce the source of C atoms required to improve diamond deposition, increase coating delamination at the subsurface level and increase the brittle failure vulnerability of coated tools [8, 9]. However, techniques such as substrate scratching with diamond powder (~ 0.5 µm) and the use of interlayers such as titanium nitride (TiN) effectively increased diamond nucleation, resulting in a diamond with well-faceted morphology and crystallinity. As a result, in the hot filament chemical vapor deposition (HFCVD) technique, a continuous and uniform coating promotes good coating adhesion [10, 11]. Furthermore, the results demonstrated that a higher activation energy barrier must be overcome for the heterogeneous nucleation process to proceed inside chemical vapor deposition (CVD). As a result, substrate pre-treatment lowers the activation energy, increasing nucleation density and forming a uniform coating over the substrate surface. Furthermore, thin-film formation includes the procedures for condensing diffusing particles and forming particle–particle clusters on the substrate surface. The particle's nucleation, growth, and coalescence determine the particle's shape, size, and distribution on the surface. The increased diffusing particles produce a continuous coating on the substrate due to a high but optimized nucleation density [12–15]. As a result, the crystallinity and homogeneity of diamond particles, which influence the film's mechanical properties, are known. The formation of microcrystalline diamond (MCD) crystals necessitates a constant supply of CH_3 radicals. As a result, parameters such as the CH_4 (methane) and H_2 (molecular hydrogen) ratio play an active role in the formation of MCD crystals with well-faceted and columnar structures [16, 17]. Non-diamond crystals result from a lack of hydrogen ions (H^+), whereas a stable plasma intensifies the nucleated crystals. Varying the concentration of H^+ ions from increased to excess results in coarser nucleated to coarser faceted (100) MCD crystals. Maintaining an optimal gas supply results in a smooth transition from (100) MCD crystals to (111) individual faceted MCD crystals suitable for industrial applications. As a result, different crystal orientations produce different surface film textures [18].

The decomposition of hydrocarbon precursors by the impact energy (ion energy) of impinging atoms in the substrate strongly influences sp^3 bonding in the film. The low ion energy results in soft polymer-like carbon films due to an open structure of unbounded H_2. Maintaining intermediate ion energy causes sufficient hydrocarbon precursors to break up, reducing H_2 resulting in diamond-like carbon (DLC) film with high sp^3 bonds. On the other hand, excess ion energy increases graphite-like bonds as the number of sp^2 C atoms in the film increases [19]. Therefore, optimal H_2 content in deposited films ensures the formation of C–H bonds (stronger than C–C bonds) through the passivation of dangling σ-bonds in carbon atoms. This results in less interfacial coated tool-workpiece adhesion, resulting in lower friction and maximum structural resistance to coatings while performing mechanical operations across the film at high temperatures [20]. During mechanical applications, diamond-coated tools frequently experience layer delamination. As a result, the diamond grains' size and surface texture (fine or coarse) determine the coating's adhesion strength [21, 22]. The increased bonding area between the film and the substrate at the interface (due to proper diffusion of carbon and cobalt atoms at the interface) combined with decreased voids in the film improves the mechanical properties of the coated sample [23]. Furthermore, the film's resistance to crack propagation from the impact force of the indenter evaluates the film's adhesion quality. The indenter force generates tremendous shear stress at the sample's contacting interface, resulting in localized stress concentration regions at the interface. As a result, the samples' fatigue resistance and adhesion at the interface zone are reduced [24]. The process introduced cracks into all of the samples, which propagated through the weak planes of the film–substrate interface, eventually leading to layer separation at the interface. The delamination is affected by the crack propagation and the distribution of stresses at the interface zone [25, 26].

Very few reports cited the detailed growth of diamond crystals on SPUN (tungsten carbide (WC) coarse grain with 6% Co as a binder) cemented carbide inserts using HFCVD while maintaining the same operating conditions for all eight different TM powders. Although previous reports have emphasized other CVD techniques for diamond nucleation, residual stresses in films affect the quality of machined surfaces. HFCVD becomes an effective means for the nucleation and growth of diamond on the non-diamond substrate without using interlayers. This paper attempts to develop diamond crystals using an alternative seeding powder to diamond powders. Furthermore, the primary goals were to determine the topological characteristics, surface roughness, and adhesion quality of the samples after coating. The film was characterized by sp^3 and sp^2 carbon bonding, which correlated mechanical properties to machining non-ferrous alloys.

2 Experimental procedure and conditions

The substrate was pre-treated with trichloroethylene and acetone to remove any unwanted particles. The etching procedure was carried out for 10 min at room temperature using

ultrasonic vibration (2200 MH, Frequency 45 kHz, Sonica, Italy) and the reagent ($HCl + HNO_3 + H_2O$) in a (1:1:1) ratio. As a result of this pre-treatment, small voids form on the substrate surface. Furthermore, any diluted cobalt from the surface was removed by ultrasonically cleaning the sample for 15 min with deionized water. Following that, the substrate was ultrasonically seeded with eight micro powders (GC, Ta, Mo, Dia., Pd, Pt, Ir, and W) for 5–10 min, as shown in Table 1. During the seeding procedure, a moderate amount of seeding powder was mixed with isopropanol and allowed to seed ultrasonically in a borosil beaker. So, we took precautions to ensure the availability of minimum seeding powder for seeding purposes. The seeding powder should not fill the void or cavity. The samples were ultrasonically cleaned for 3 min with isopropanol alcohol to remove the surplus seeding powder. As a result, the process improves nucleation density to a greater extent.

The diamond deposition was carried out using an HFCVD setup. Table 2 displays the process parameters for diamond deposition. A single Ga–As laser (630–670 nm, 5 mW) infrared pyrometer was used to control the tungsten filament temperature (3i1ML2, Raytek, USA). A molybdenum heater was used to heat the substrate. A K-type thermocouple was used to measure the temperature of the substrate. During deposition, this was about 5–6 mm away, directly underneath and touching the bottom of the substrate. However, the actual temperature on the insert's surface is 100 ± 20 °C higher than the measured temperature. Mass flow controllers were used to introducing the reactant gases H_2 and CH_4 into the HFCVD chamber (model 1179A and 1179B MKS Instruments, USA). A Baratron pressure sensor was used to keep the deposition pressure constant (model 627B, MKS Instruments, USA).

Surtronic S128 Talysurf (Taylor Hobson, UK) measured surface roughness after pre-treatment [27]. After each operation, the mean surface roughness (R_a), average peak to valley height (R_z), and maximum roughness (R_{max}) were measured. All tests were carried out with a cut-off length of 0.8 mm, an evaluation length of 4.0 mm, and a range of 100 µm. All micrographs were examined using a scanning electron microscope (SEM) SU3500 (Hitachi, Japan) equipped with an energy dispersive X-ray spectroscopy (EDS) OXFORD INCAX (Oxford, UK). The 3D and 2D micrographs and the line profile and line histogram of the coated samples were examined by atomic force microscopy (AFM) using an XE-100 Park systems microscope (South Korea). The non-contact mode was used to scan at a rate of 0.5 Hz and generate the quantitative parameters on a 5 µm × 5 µm scanned area. The AFM software using the grain analysis tab determined the grain's length, standard area, perimeter, volume, and mean area. The crystal planes were determined using X-ray diffraction (XRD) (PANalytical's X'Pert, Netherland)

Table 1 Symbolic representation of carbide inserts seeded with different-sized powders

Symbol	Powder seeded diamond coating tools
T1	Tool 1 seeded with Glassy carbon powder (2–12 µm) 99.95% pure, Sigma–Aldrich
T2	Tool 2 seeded with Tantalum powder (44 µm) 99.9% pure, Sigma–Aldrich
T3	Tool 3 seeded with Molybdenum powder (1–2 µm) 99.9% pure, Sigma–Aldrich
T4	Tool 4 seeded with Diamond powder (0.50 µm) 99.9% pure, Sigma–Aldrich
T5	Tool 5 seeded with Palladium powder (< 1 µm) 99.9% pure, Sigma–Aldrich
T6	Tool 6 seeded with Platinum powder (0.15–0.45 µm) 99.9% pure, Sigma–Aldrich
T7	Tool 7 seeded with Iridium powder (≈ 1 µm) 99.9% pure, Sigma–Aldrich
T8	Tool 8 seeded with Tungsten powder (0.66–1 µm) 99.9% pure, Sigma–Aldrich

Table 2 Description of deposition parameters

Deposition parameters	
Substrate	WC-6 wt% Co ISO K10 SPUN Sandvik Cormant cemented carbide insert
Filament	Tungsten wire (ϕ 250 µm, 99.9% purity, Sigma–Aldrich) carburized
Filament temperature	2050 ± 50 °C
Seeding powder	Glassy C, Ta, Mo, Dia., Pd, Pt, Ir, W Powder
Filament to substrate distance	10 mm
Substrate temperature	700 ± 20 °C
Gas composition	1% CH_4 in H_2
Chamber reaction pressure	20 Torr
Deposition time	8 h

having a source of X-rays as Cu K-α (λ: 1.540598 Å) with diffraction angle 2-theta varied between 20° and 100°. The purity of the diamond coatings and the residual stresses were determined using Micro-Raman spectroscopy (μ-RS) [Excitation source: Argon–Krypton mixed ion gas laser, Model 2018 RM, Spectrometer: Model T64000, Detector: thermoelectric cooled front-illuminated 1024 256 CCD. Model SynpseTM (Jobin Yvon Horiba, France)]. Field emission scanning electron microscopy (FESEM) examined the cross-sectional film morphology (Zeiss Supra 55, Germany). The microhardness was measured using a digital microhardness tester (Model-MMT-X7B, Matsuzawa, Japan) equipped with a Vickers diamond indenter. With a 10 N load, a loading time of 15 s was used.

3 Results and discussion

3.1 Effect of pre-treatment on the surface roughness of the cemented carbide insert

The chemical etching process removed Co from the surface, making it rougher for powdered seeds to deposit and creating sites for incoming activated precursors in HFCVD to adsorb and increase the nucleation rate. The deep valleys increased roughness and produced large diamond growth centers, which resulted in diamond film. The increased roughness values of R_a, R_z, and R_{max} in Fig. 1a indicates the etched corrugated substrate surface. During the diamond deposition stage, the corrugated surface allows mechanical interlocking of the deposited film with the substrate. EDS measurements in Fig. 1b, c revealed that the carbon percentage on the bare SPUN insert was high before substrate etching. The presence of WC phases and amorphous carbon was attributed to the high carbon percentage. The untreated substrate was smooth, with few visible marks. The etching process resulted in substrate decarburization and decreased Co/W ratio. The substrate has several holes or deep valleys because of the preferential Co removal from the surface caused by etching. The preferential removal of Co and unaffected WC under ultrasonic vibration is due to WC's higher absorption coefficient and its higher boiling and melting temperatures than Co.

3.2 Effect of different TM powders on the surface chemistry of the substrate leading to diamond growth after the HFCVD process

Figure 2 shows the possible different stages of diamond nucleation. Figure 3 shows the surface morphology of each seeded WC-6 wt% SPUN insert following the diamond deposition stage, as well as the size of the diamond crystal generated using SEM. Figure 3a shows small-sized diamond crystallites surrounding the large-sized faceted diamond grains. Under the deposition conditions, the Co etching caused by atomic hydrogen (H^+) formed gaseous hydrides (H^-). As a result, C_2 entered the C–H bond of methane without encountering any energy barriers. The high emission intensity of C_2 dimers and the low activation energy of methane produced larger crystal structures of diamonds [28, 29]. Furthermore, CH_3 radicals combining rapidly with the C seeded substrate generate a regular C_4 bond in the nucleating site, promoting increased diamond crystal growth. The higher percentage of C turning into diamond leads to secondary nucleation, resulting in the formation of smaller crystals around the larger ones. Figure 3b showed sufficiently

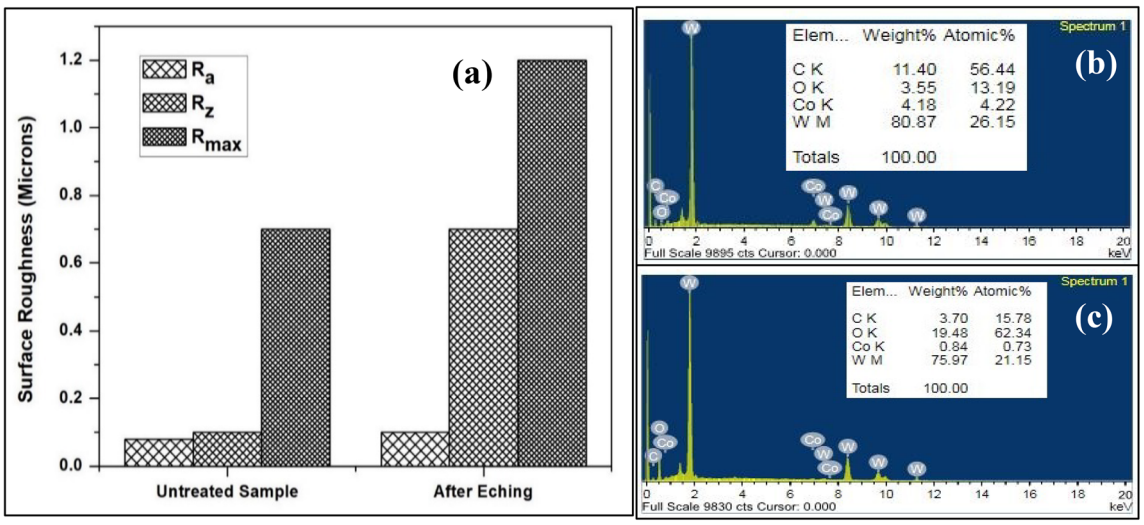

Fig. 1 Roughness parameters for untreated and pre-treated WC–Co substrates (**a**) and EDS for unetched and etched WC–Co substrates (**b**) and (**c**), respectively

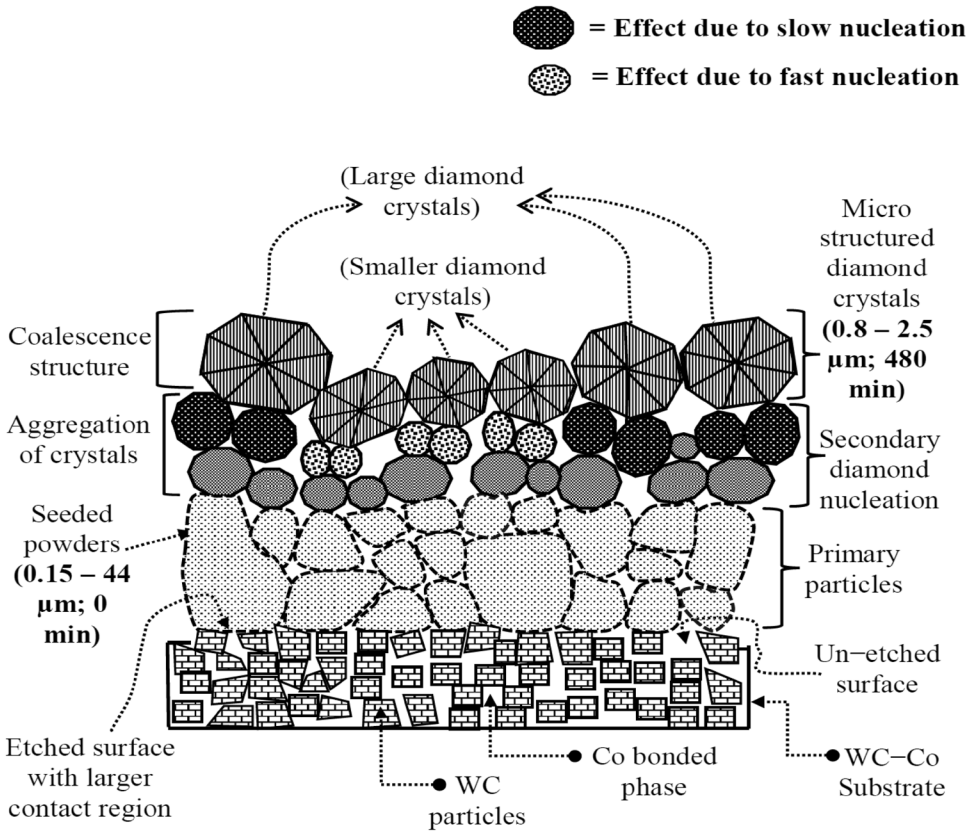

Fig. 2 Schematic illustration of the MCD particle nucleation and growth process

large homogeneous well-faceted nucleated crystals (~ 60) with Cubo octahedral shapes. The cross-section revealed uniformly distributed crystal growth. On average, diamond crystals formed have a size of about 2.2 µm. Each particle is joined together to form a continuous growth of diamond crystals. The XRD graph clearly shows the reaction mechanism of Ta powders with cemented carbide catalysed tantalum carbides (TaC/Ta_2C) intermediate phases. The Ta_XC phase acts as a barrier to C diffusion and saturates it on the surface. Therefore, the growing diamond film on the substrate had a higher excited state of electrons with C–C bonds, promoting Csp^3 atoms. Diffusion of Co at the WC/Co interface resulted in a decrease in Ta–carbide bonds because no $CoTa_2$ alloy was formed [30, 31]. Figure 3c shows discrete diamond crystal formation with roughly half the number of crystals compared to tantalum powders, attributed to the diamond nucleation's moderate micro-sized Mo seeds. On the other hand, the formation of Mo_2C at the substrate surface triggered the accumulation of C at the surface, resulting in C–C bond formation and rapid diamond nucleation, with the coating's adhesion strength expected to be high [32, 33]. Figure 3d shows diamond crystals nucleated with an average growth rate of 0.3 µm/h with moderately scattered crystals. The diamond crystals formed were more faceted and continuous. Secondary nucleation was responsible for the scattering of diamond grains. An ordered lattice structure of diamond-shaped crystals indicates that the ions accountable for diamond growth form chemical carbide bonds faster near the nucleating surface.

The non-epitaxial crystal growth, as seen in Fig. 3e, is responsible for producing large cauliflower-shaped diamonds with no definite facets. There is a non-homogeneous growth of crystals ranging from larger to smaller. The reason is, during the diamond nucleation and growth stage, an insufficient number of aggregated smaller particles converted into large-sized particles due to coalescing. Diamond crystal formation was predominantly triggered by the rapid diffusion and super-saturation of H^+ ions through Pd seeded powders with dissolved C tending to precipitate on the substrate surface as a graphitic layer [34, 35]. Figure 3f depicts a textured diamond growth pattern throughout the substrate, with remarkably few minuscule micro-sized diamond particles. Since Pt dissolves less than 1% of solid carbon at temperatures between 700 and 850 °C, few C radicals diffused into Pt, while some saturated at the surface. The lack of maximum C at the substrate surface resulted in low energy on the film surface. The film was bombarded with low-energy H^+ ions, resulting in decreased Csp^3 atoms. The CH_4/H_2 plasma that formed the Pt–C–H phase contributed to a few diamond particles in the film. As a result, the small size and a low number of crystals formed are related to particles mostly remaining in the nucleation stage and only a few converting

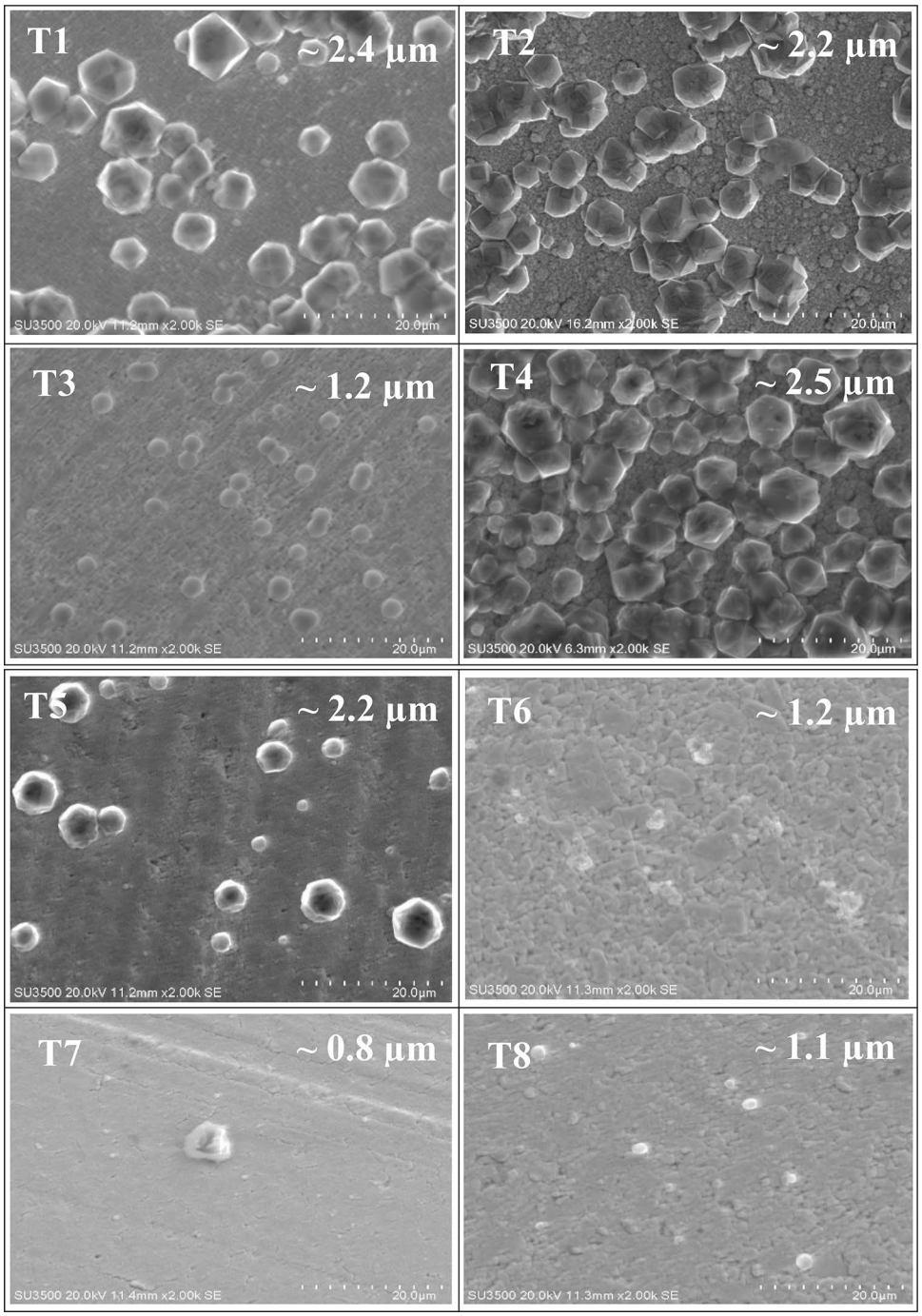

Fig. 3 Microstructures of inserts generated by the HFCVD process seeded with different transitional metal powders and the size of the diamond crystal formed

to diamonds inside HFCVD. Figure 3g indicates that the use of iridium powder resulted in discrete and very few numbers of diamond crystals. A coalesced diamond formed into a single crystal in a few areas of the film surface. Diamond particle coalescence was caused by the formation of the smallest-sized particles (~ 0.8 µm), which increased their collision frequency and mobility. However, due to insufficient carbon coalescence in iridium, there were few nucleating sites for diamond, with grain boundaries forming a thin epitaxial film [36]. Figure 3h shows the formation of a small number of scattered diamond grains. The reason being the low mean free path created from the filament to the substrate inside the HFCVD chamber resulted in low surface adsorption of carbon atoms. The active radicals (CH_3 and H_2) collided more frequently, resulting in kinetic energy (K.E.) loss during deposition. The decrease in H^+ ions resulted in a lack of nucleating sites, making the conversion from sp^2 to sp^3 phase difficult.

Diamond crystals with Cubo octahedral, cauliflower, and spherical shapes were discovered in the (T1, T2, T4), T5 and

(T3, T6, T7, T8) samples, respectively. The diamond crystal sizes for T4, T5, T6 and T8 samples are larger when compared to the seeded powders used for nucleation. As a result, the growth rate of diamond crystals in the samples reported above was unaffected by simultaneous Co production during the deposition process. The diamond crystal sizes formed in the T1, T2, T3, and T7 samples were smaller than the original powder size. This is because increased super-saturation of C on the surface causes more secondary nucleation, which prevents the growth of a single-crystal diamond. On the other hand, the ratio of the maximum ($D_{max} \approx 2.5$ µm) to the minimum ($D_{min} \approx 0.8$ µm) size of diamond crystal formed was found to be 3.125. The larger diamond crystal diameter of around 3.125 µm indicates heterogeneous nucleation because the average sizes of crystals formed were either larger or closer to the size of the seeded powders used [37].

The time it takes for TM powders to complete the formation of individual diamond crystals is shown in Fig. 4. Since the size of diamond grains increases with time [38], the time used for deposition is considered to be the maximum time required for the complete formation of the largest diamond particle (2.5 µm) (480 min). Compared to the maximum time assumed, the corresponding time for the growth of diamond particles of various TM powders to their respective sizes is computed. The SEM pictures reveal that, compared to samples T1, T2, T4, and T5, samples T3, T6, T7, and T8 have smaller diamond crystals. This is because the latter samples have quicker nucleation rates, resulting in the shortest time required for the complete growth of a diamond crystal.

3.3 Characterization of the MCD film deposited on a cemented carbide substrate

A Lorentzian fit for all of the Raman figures shown in Fig. 5 indicated the presence of a vibrational mode in the deposited film. The minimum scattering from the natural diamond peak in the sample (T1) resulted in the Raman band of 1331.94 cm^{-1}. However, the overall intensity is lower compared to T2, T3, and T4 samples, and the FWHM value is higher when compared to T2 and T4 samples. The breaking of C–H bonds due to increased ion energy striking the substrate, evident from the lower sp^3 intensity band, could be the reason. The 1585.27 cm^{-1} peaks are described as a diamond-like a-C: H (DLCH) graphite band caused by an increase in π-bonded carbons at the MCD grain boundaries. As a result, C–C bonds were replaced by C–H bonds. As a result, lower sp^3-bonded carbon atoms are expected in the film. The second sample (T2) exhibited a sharper, higher intensity peak at 1335.45 cm^{-1}, with the least scattering from the natural diamond peak on the positive side and the smallest FWHM value. As a result, the Ta sample has more sp^3 bonds in the film. The G-Peak indicated the formation of hydrogenated amorphous carbon (a-C: H) content in the film with graphitic impurities. The D-band peak in the sample (T3) at 1326.93 cm^{-1} corresponds to hydrogenated amorphous carbon, and the G-band peak at 1565.41 cm^{-1} corresponds to amorphous carbon (a-C) in the film with sp^2 chain structures (olefins) changing to the ring structure. The sample has the highest lattice expansion for diamond crystals and wider peak intensity for D and G bands. Peak broadening is attributed to phonon dispersion at grain boundaries and non-uniform growth surfaces. The C atoms' increased bond length is demonstrated by a shift in the Raman band to lower wavenumbers, where Csp^2 atoms are expected to surround sp^3-bonded atoms. The diamond band to sp^2 characteristic band ratio in the sample (T4) was higher and comparable to that in the T1 and T2 samples. With very low compressive stresses in the film, the diamond peak deviation was less positive and similar to the T2 sample. The increase in H_2 and H saturation in C=C

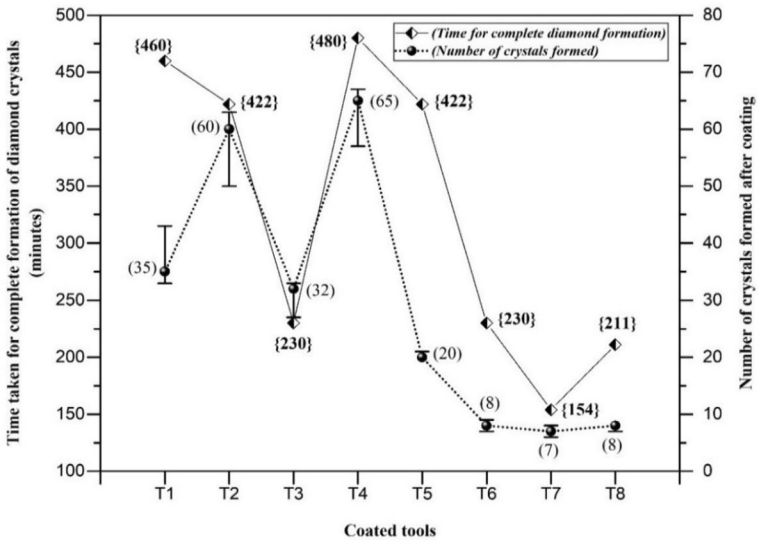

Fig. 4 Individual sample time for their corresponding crystal size vs. the number of crystals formed for each sample

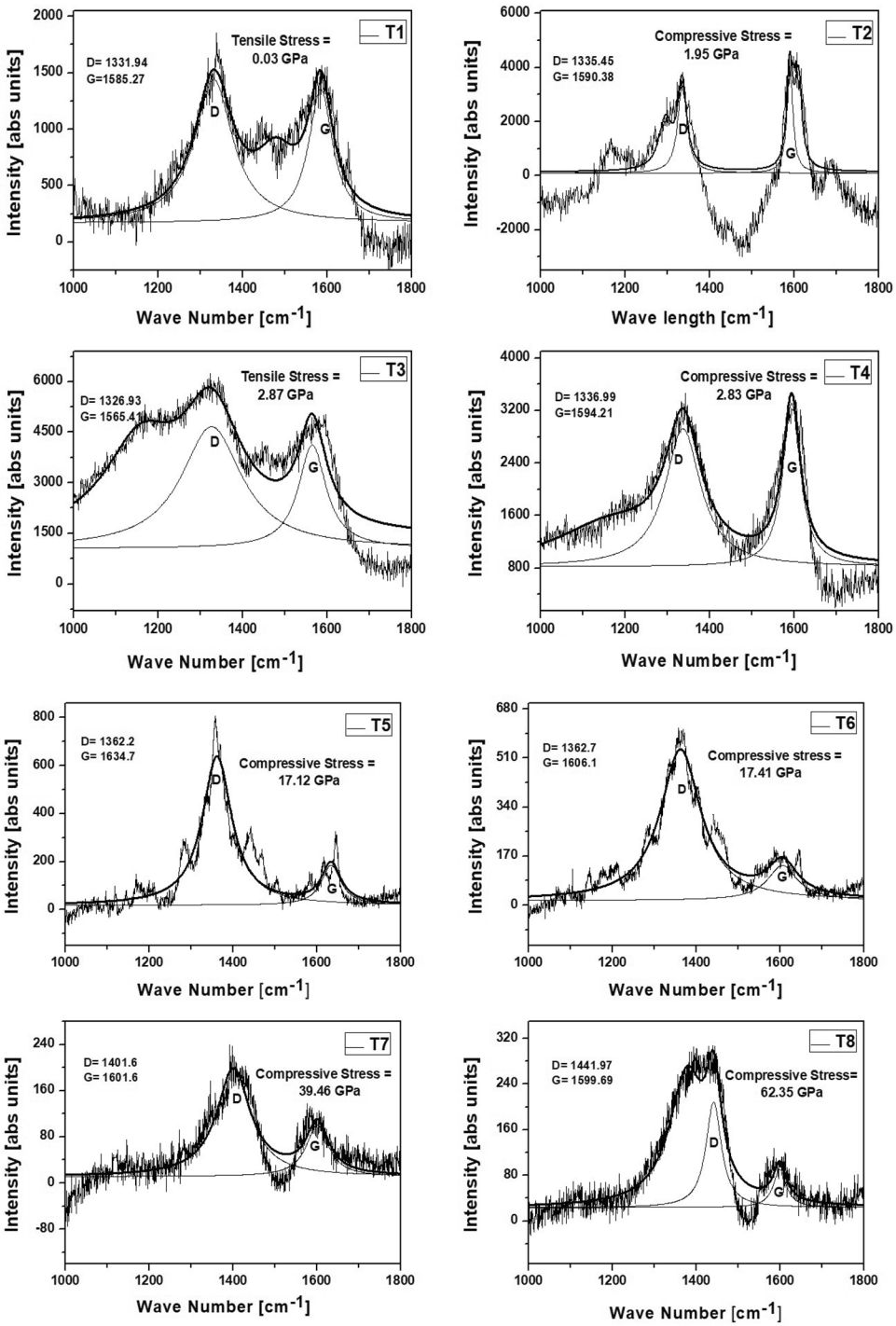

Fig. 5 Images of Raman spectra for the coated substrate with various powders and their Raman shift values in GPa

bonds would have increased the number of sp^3 carbons in the film. The G band at 1594.21 cm^{-1} was assigned to a-C: H in the film.

The peak at 1362.22 cm^{-1} in the sample (T5) exhibited the maximum diamond intensity among the T5–T8 samples, indicating large grain sizes of diamond crystals with dense diamond coatings. The G mode at 1634.68 cm^{-1} indicated the presence of (a-C: H) with a polymeric structure. The increase in G-peak position beyond 1600 cm^{-1} was attributed to the formation of sp^2 carbon chains. The Raman spectra for sample (T6) were more intense than those for sample (T5). However, two broad bands were observed at 1362.7 cm^{-1} and 1606.1 cm^{-1}, corresponding to the D (disorder) and G (graphitic) bands, respectively. The D-peak indicated sp^2 site breathing modes in rings. The G-peak, which was formed by aromatic hydrocarbons or C=C chains formed during the

deposition stage and condensed on the growing diamond surface, indicated the presence of an a-C content. A higher wavenumber describes higher sp^2 carbon vibration modes in the film for G-peak of around 1606.1 cm^{-1}. The sample (T7) showed the lowest diamond intensity peak. The characteristic peaks at 1401.6 cm^{-1} indicated the formation of microcrystalline graphite (µc-G), composed of polymeric aromatic hydrocarbons with two-dimensional (2D) ππ conjugated planar structures. The G-peak indicated the presence of a-C: H in the film with an sp^2 ring-like structure. The D-peak at 1441.97 cm^{-1} was attributed to a hydrogenated analogue of tetrahedral amorphous carbon (ta-C: H) content in the film, which had sp^3 CH_3 asymmetric ring and sp^2 CH aromatic ring-like structures. The G-peak revealed a diamond-like structure (a-C: H). As a result, when the H or sp^3 content is high, the substrate transitions from polymer to diamond-like film.

The residual stresses in the film revealed the diamond film's quality. The equation is used to compute the residual stresses (σ) in the film, which are represented as [39]:

$$\sigma = -0.567\left[V_m - V_o\right] \text{ GPa} \quad (1)$$

$[V_m - V_o]$ = difference between measured peak position and Raman peak shift for an unstressed diamond film (1332 cm^{-1}).

The differences in thermal expansion coefficient (α) between tantalum carbide ($\alpha = 6.64 \times 10^{-6}$ K^{-1}) and diamond formed ($\alpha = 1 \times 10^{-6}$ K^{-1}) cause residual stress in the film. According to Fig. 5, all samples exhibited compressive stresses for the film, except for the T1 and T3 samples, which exhibited tensile stresses, resulting in diamond lattice expansion. A higher compressive stress value in T5, T6, T7, and T8 samples destabilises the sp^3 CH_x groups in the film, reducing diamond purity. Residual stresses in the film affect the full width at half maximum for D-Peak ($FWHM_D$) of Raman spectra. Table 3 shows that a low $FWHM_D$ value correlates with high crystallinity and large grain size of formed diamond crystals [40]. The order of crystallinity in the diamond film is related to: T2 > T8 > T5 > T7 > T4 > T1 > T6 > T3. Therefore, sample T2 exhibited higher crystallinity with columnar crystal growth. The disoriented structure affects the full width at half maximum for G-Peak ($FWHM_G$) due to the higher bond angle and bond length of sp^2 C atoms due to an increase in sp^3 clusters. The amount of a-C in the film raises $FWHM_G$, which causes the least amount of disruption to the sp^2 sites. This makes Csp^2 to Csp^3 phase conversion difficult [41]. The I_D/I_G ratio (intensity ratio between D-peak and G-peak) reflects changes in film microstructure, with a higher value indicating the size of non-diamond planes or sp^2 phases in rings [42, 43]. The increase in a-C grain size increases Csp^2 content in the film, as evidenced by the higher I_D/I_G ratio, and the order in our case is T2 < T1 < T4 < T3 < T7 < T8 < T5 < T6. The T2 sample has the least disorderly film, indicating higher diamond planes. In the film, samples T5 and T6 encountered higher graphite phases with larger aromatic clusters. The *x*-factor [44] was used to investigate the diamond-to-non-diamond ratio in the film.

$$x = 100 \times \frac{\left(75 \times I_{diamond}\right)}{\left(75 \times I_{diamond}\right) + I_{non-diamond}} \quad (2)$$

where $I_{diamond}$ and $I_{non\text{-}diamond}$ represent area under diamond and non-diamond peaks respectively.

The samples with the fewest deviations in grain sizes, as all of them, had *x* values in the range of (98.64–99.76). Higher *x* values are associated with larger grain sizes of diamond crystals with MCD tendencies and minimum grain boundary density and sp^2 carbon content. Smaller grain sizes are found in samples T2, T1, T4, and T3 when compared to samples T5, T6, T8, and T7. Smaller grain sizes indicate diamond crystal formation with higher nucleation densities and, as a result, higher coating adhesion.

According to the SEM and Raman results, samples T5, T6, T7, and T8 had fewer diamond crystals and a higher I_D/I_G ratio than samples T1, T2, T3, and T4. As a result, the former samples contained more amorphous carbon than diamond crystals, the XRD and AFM analysis were not carried out.

As shown in Fig. 6, XRD for all four samples resulted in a higher intensity of the (111) plane compared to the (220)

Table 3 Peak properties of the Raman spectra

Samples	Pos D (cm^{-1})	FWHM D (cm^{-1})	Pos G (cm^{-1})	FWHM G (cm^{-1})	I_D/I_G	*x*
T1	1331.94	109.22	1585.27	70.05	1.67	99.21
T2	1335.45	26.13	1590.38	17.23	1.29	98.98
T3	1326.93	174.41	1556.41	79.76	2.57	99.48
T4	1336.99	102.38	1594.21	50.45	1.71	99.22
T5	1362.22	85.15	1634.68	56.29	5.61	99.76
T6	1362.72	116.4	1606.13	87.70	5.69	99.76
T7	1401.65	97.49	1601.69	64.96	3.13	99.58
T8	1441.97	44.50	1599.69	37.75	3.29	99.59

and (311) planes. The strong CH_2–CH_2 covalent link of the CH_4 molecule present at the (111) plane and the lowest surface energy at the (111) plane, diamond growth at the (111) crystal face was the fastest compared to other planes [45]. As a result, the diamond powder produced higher facetted cubic crystal structures and lower octahedral crystals in the film (T4 sample). (111) oriented crystal growth results in heteroepitaxial coalesced diamond films with defect-free film surfaces. The crystal's preferred growth orientation indicates the formation of a thicker film. Diamond growth along [111] or [100] promotes cubic or octahedral crystal growth, respectively, whereas any intermediate planes between these two planes promote Cubo octahedral crystal growth.

The 2D images in Fig. 7 show a topological change in the surface structure of the thin MCD film with different grain sizes and grain shapes between the four samples. Due to the slow nucleation process, the (T1) sample had an uneven clustered distribution of particles with few void formations between the MCD clusters. As a result, crystal growth in T1 samples took a long time. Due to the coalescence of smaller particles, densely populated MCD particles are distributed in the (T2) sample, resulting in very homogeneous and continuous layers of diamond crystals. The increased interlocking of tantalum seeds with the substrate caused this. As a result, more diamond particles are available for subsequent diamond growth via the HFCVD process. In the (T3) sample, clustering of large non-uniform particle distribution with individually separated diamond grains was observed. The particle distribution in the (T4) sample was discrete granular clusters with a lower formation limit. The multiple nucleations on a single particle during diamond formation caused this.

The maximum height of the peak for the T1 (< 100 nm) and T2 (~ 200 nm) samples is significantly lower than for the T3 (~ 300 nm) and T4 (~ 400 nm) samples, as shown in the 3D image. It is also discovered that the decrease in peak maximum height in T1 and T2 samples are caused by an increase in several microparticles on the surface. This increases film adhesion by increasing the interfacial bonding of the film and substrate due to van der Waals forces. Because of these interactions, the surface becomes smooth, and the roughness values ((R_a) and root mean square roughness (R_{rms})) are affected. The higher height values in the T3 and T4 samples, on the other hand, indicate large peaks and valleys, which raise the R_a and R_{rms} values.

The negative R_{sk} (surface skewness) distributions for T1 (− 0.242), T3 (− 0.097), and T4 (− 0.53) samples indicate that the film has many cracks and porous surfaces. The T2 sample's positive R_{sk} value (0.045) demonstrated that the scanned surface area has: (a) more peaks than valleys with a homogeneous distribution; and (b) the highest contact force at the interface, resulting in the highest coating adhesion.

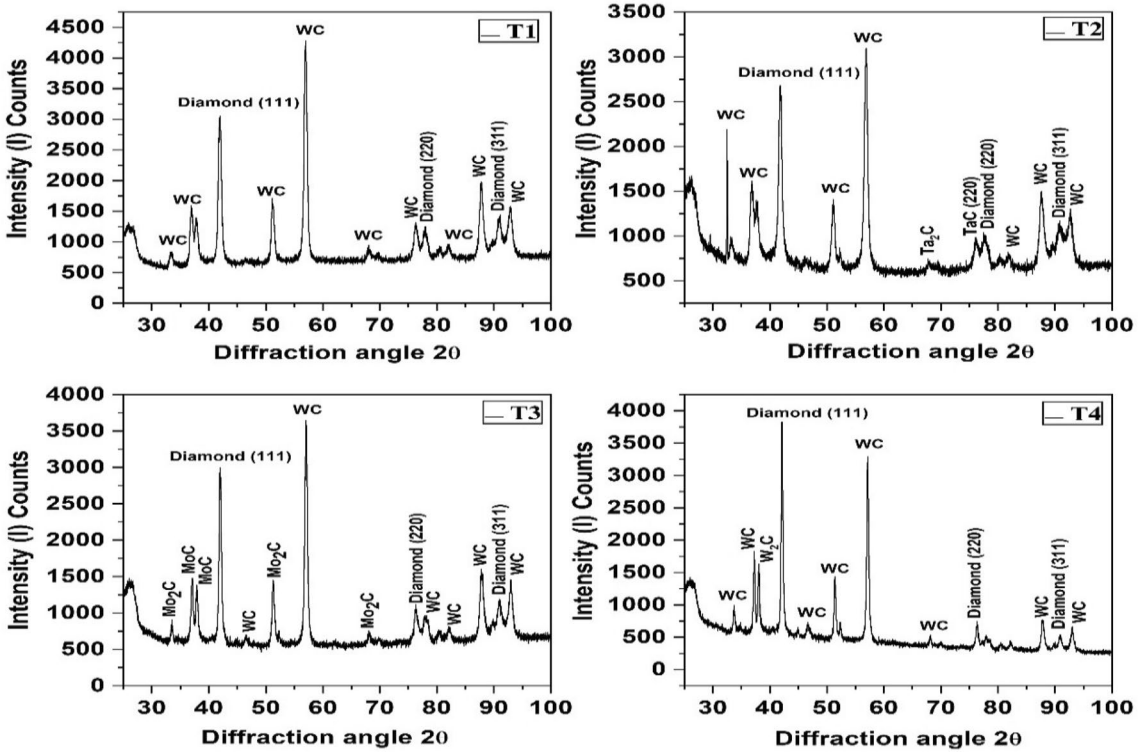

Fig. 6 XRD pattern of coated SPUN cemented carbide inserts

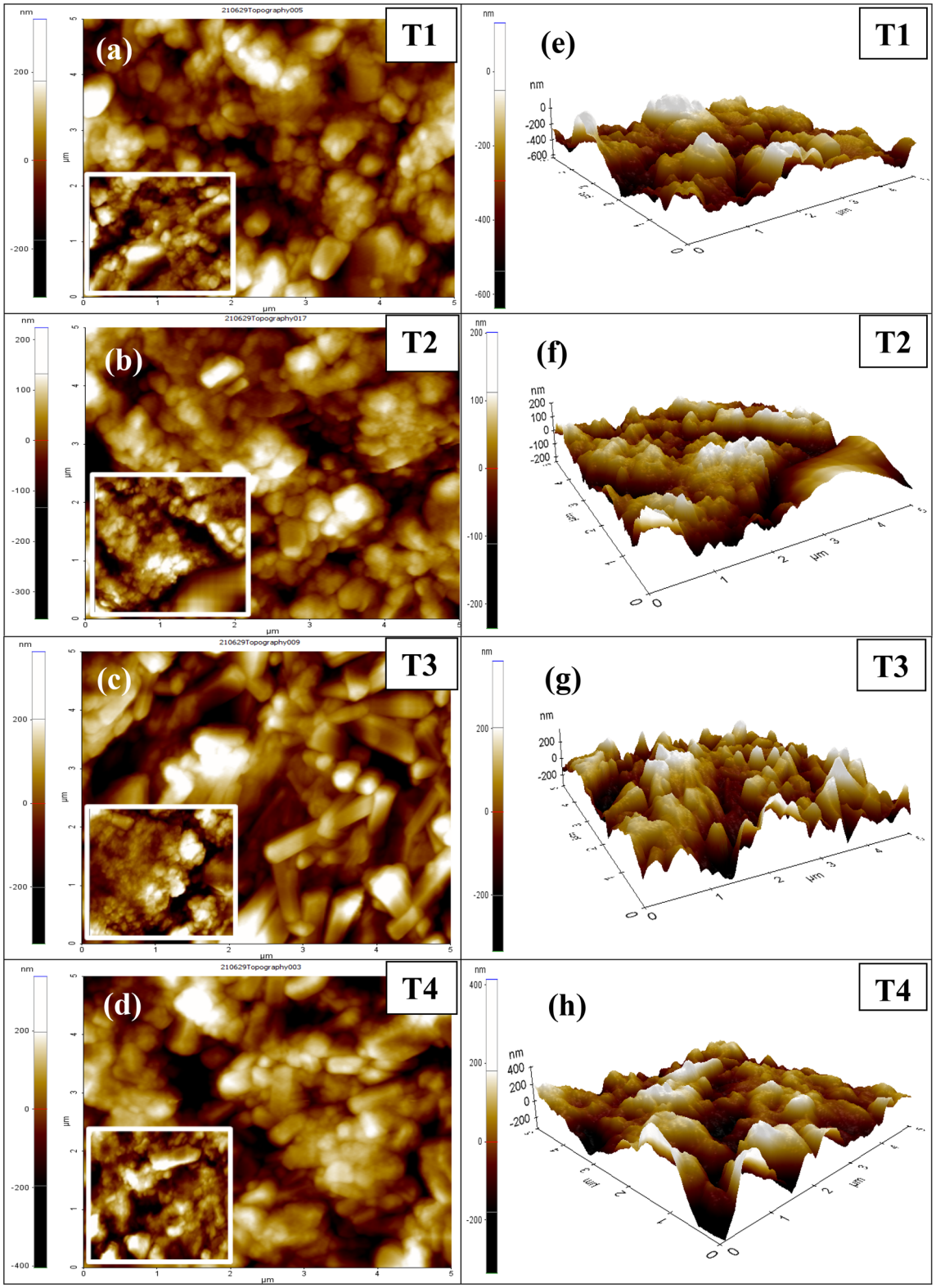

Fig. 7 The 2D and 3D AFM topographical images of the grain distribution for the coated samples are shown in (**a**)–(**d**) and (**e**)–(**h**), respectively

The R_{ku} (kurtosis value) for the T2 sample was the highest (2.83), followed by the T4 sample (2.48), indicating that the surfaces had more diamond peaks and fewer valleys than the T1 (1.77) and T3 (2.38) samples. Since all samples had R_{ku} values of less than 3, the surfaces had fewer diamond peaks and more valleys with more irregular surfaces. The T3 (751.24 nm) sample had the highest R_{pv} values (the difference in minimum and maximum values in the selected region), indicating that the surface valleys are longer and deeper. As a result, non-homogeneous particle distribution is expected in T3 when compared to T1 (460.36 nm), T2 (332.77 nm), and T4 (487.63 nm).

Figure 8 shows that T1 and T2 samples had lower R_a, R_{rms}, and R_{max} (peak to peak distance) values than other samples, indicating a less rough diamond film with small grain sizes of diamond particles. T4 samples had randomly distributed diamond grains, and the film surface was rougher than T2 and T1 samples due to greater R_{max} values. As a result, the T4 sample should have a large grain size and excellent film/substrate adhesion at the interface. For the T3 sample, the coarser grains with the highest R_{max} value create a rough film. The T3 sample has the highest R_a (142.15 nm), indicating a thicker film, but adhesion is reduced due to large voids at the film/substrate interface (results from R_{pv}). The R_a for the T2 sample (59.21 nm) was the lowest, indicating good adhesion properties. However, a small mean grain size (127.7 nm) generated more attractive forces among the particles, simultaneously causing voids to form on the surfaces.

The samples' surface line profile images and line histograms are shown in Fig. 9. The line profile demonstrates that the roughness parameters are directly related to the scanner's vertical movement (Z value). Surfaces with deep valleys and high peaks cause the scanner to move up and down over the required region. The surface line profile images show that the (T1) sample had more deep pits than peaks (below and above the 0 line, respectively), indicating rougher than the T2 sample. The zigzag pattern in the line profile is explained by the smaller diameter of the grain size, which causes particles to be close together. Smaller grains may indicate a more homogeneous grain distribution, but more holes on the surface make the structure more serrated. The (T2) sample exhibits a smooth pattern with fewer fluctuations, resulting in a smooth coated film surface. The lower vertical distance of ~ 130 nm results in fewer micro grains on the surface. The (T3) sample had the greatest overall roughness value, corresponding to the greatest vertical distance (400 nm). As a result, the average distance between the two peaks grows with the largest grain sizes. The line profile revealed more repeated fluctuations in (T4) samples with shorter wavelengths, indicating a rough surface. The greater vertical distance (> 300 nm) also indicates the same.

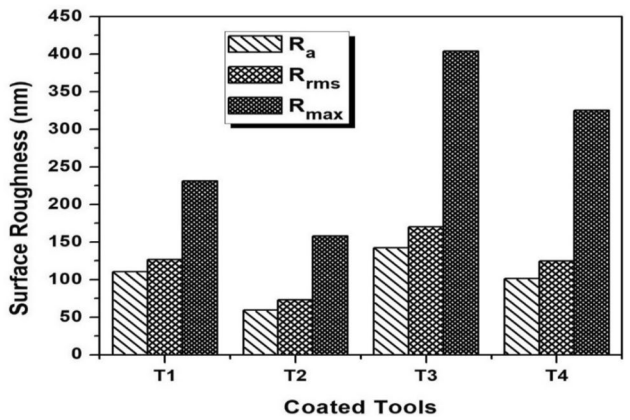

Fig. 8 AFM surface roughness parameters after coating

The line histogram shows the maximum pixel heights generated for the T4 sample. This is because the above sample has a higher surface roughness due to the large grain sizes of the particles. The roughness values of the T1, T2, and T3 samples were comparable. The increase in roughness value for the T1 sample is due to particle agglomeration with poor particle dispersion.

The histogram distribution in Fig. 10 shows that the T2 samples have broader particle distributions due to their large area (> 4 μm^2) and perimeter (> 8 μm) in the X-axis direction when compared to the other samples. This is owing to the T2 sample's more homogeneous distribution. The T2 sample has a higher units/div. (40) than the others, indicating more particles in the surface area. The grain diameter was determined using the following mathematical formula:

$$d = 2 \times \sqrt{\frac{V}{\pi l}} \ldots\ldots\ldots\ldots\ldots\ldots \quad (3)$$

where d, V, and l are the diameter, volume, and length of the grains, respectively.

Table 4 shows the average grain parameters. MCDs in the T4 sample grew in vertical (i.e., length) and lateral (i.e., diameter) directions. The mean grain diameter in the T2 sample was the largest. The aspect ratio of T2 sample was the lowest, followed by the T1 sample. T1 had the slowest vertical growth, followed by T2. As a result, smaller grain-sized particles are expected in the T1 and T2 samples. T1 and T2 samples had a broader film distribution (X-axis direction for area and perimeter for T1 and T2 were greater than for T3 and T4 in Fig. 10), indicating a higher number of particles. Moreover, a lower aspect ratio ensures the homogenous load distribution for the coated sample when acted upon by the external force. The films containing too-large grain size because of their smaller lateral size and larger longitudinal size are most likely to get broken (brittle property) when heavy operations are carried out.

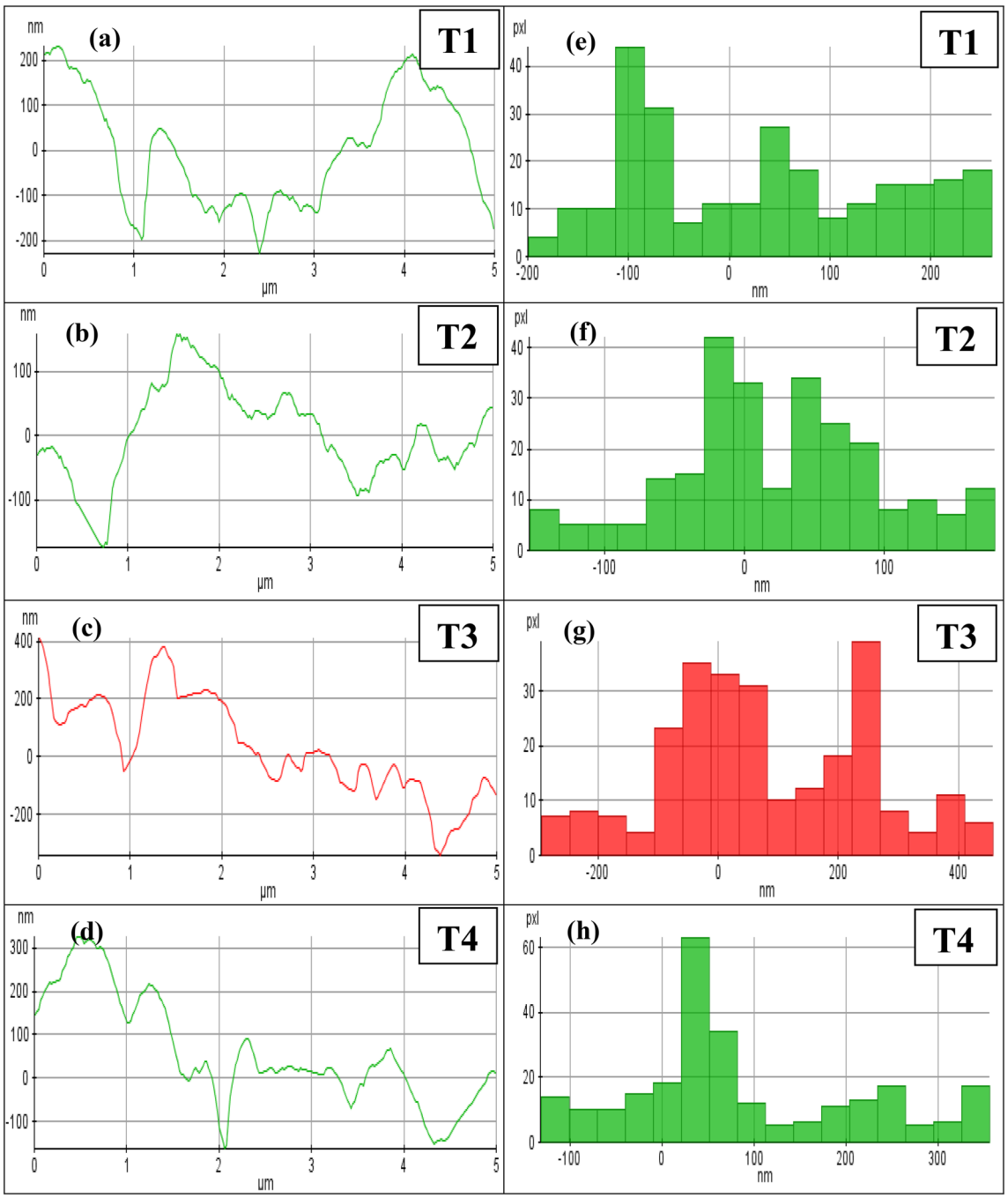

Fig. 9 The surface line profile images are shown in (**a**)–(**c**), and (**d**); the corresponding line histogram for the roughness parameters is shown in (**e**)–(**h**)

3.4 Film morphology and adhesion strength of the coatings with different seeding powders

As shown by the FESEM cross-sectional images in Fig. 11, the film morphology is rough and non-uniform for all samples. However, the films grow linearly with no buckling at the interface [46]. This demonstrates that the film grew due to increased compressive stress among the grains, resulting in a high grain packing density. As a result, the coatings in these samples are likely to have good mechanical properties. On the other hand, T3, T5, T6, T7, and T8 samples had a high number of voids. The samples could be stuck at the second stage of the diamond film's growth process (where the film does not fill the voids), with the origin being the nucleating sites. The cross-sectional morphology in the T1 and T4 samples contained a compact film (with no gaps)

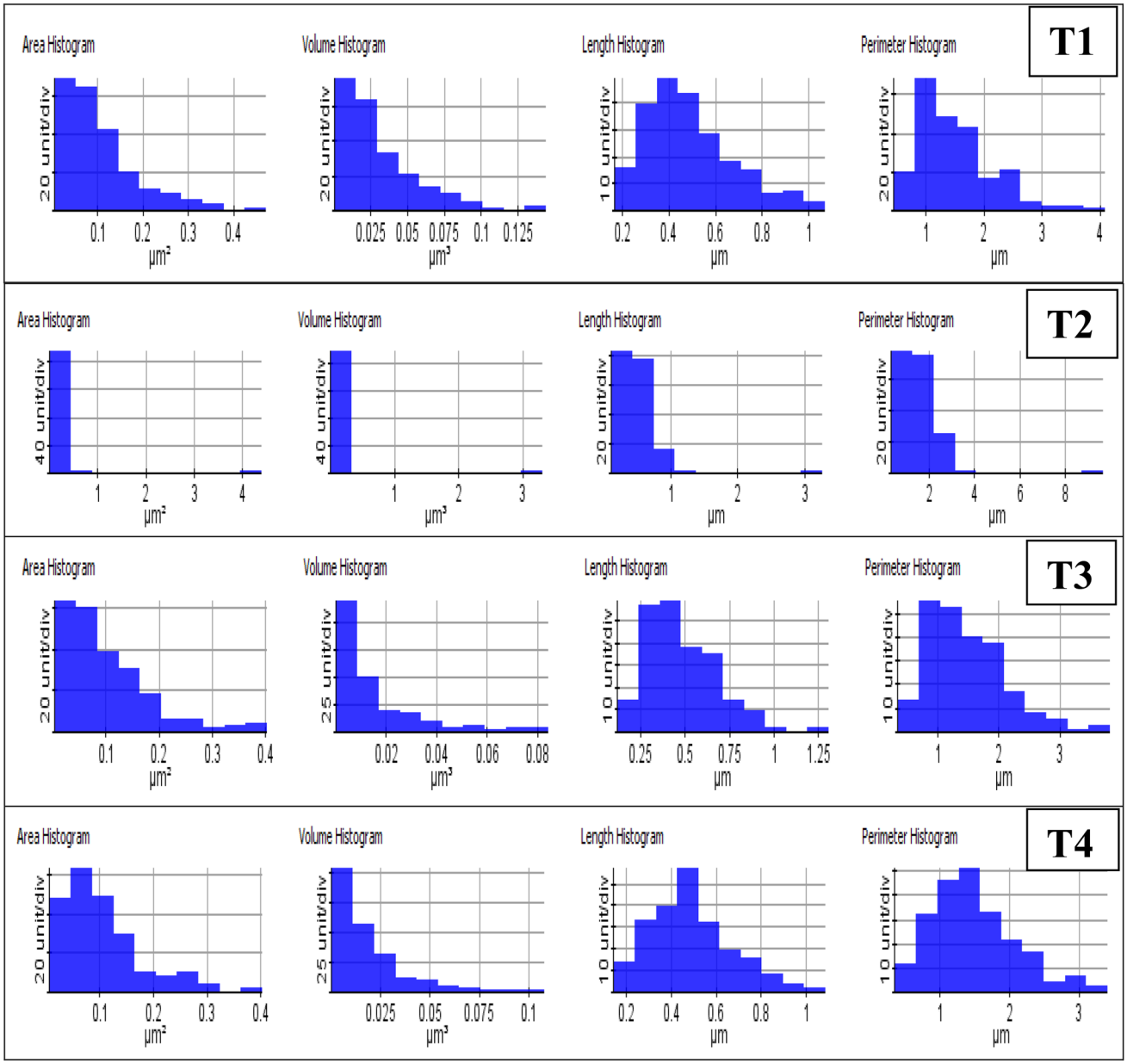

Fig. 10 Surface profile parameters exhibiting grain dispersion in the coated surfaces

Table 4 Gaussian fit values for the mean grain parameters as detected in Fig. 10 through AFM on the sample surface

Samples	Area (μm^2)	Volume (μm^3)	Length (μm)	Perimeter (μm)	Diameter (μm)	Aspect ratio (l/d)
T1	14.39×10^{-2}	6.87×10^{-2}	0.1067	0.11	0.91	0.12
T2	23.75×10^{-2}	19.52×10^{-2}	0.1277	0.34	1.39	0.09
T3	8.80×10^{-2}	8.29×10^{-2}	0.1715	0.17	0.78	0.22
T4	12.40×10^{-2}	14.69×10^{-2}	0.1665	0.03	1.05	0.16

covering the valley regions of the interface zones with the diamond grains. The T2 sample had voids, but they were smaller than other samples. As a result, for T1, T2, and T4 samples, the diffusion of coating material and substrate occurred smoothly at the interface. Because the T2 sample has a higher film thickness and no tensile residual stresses,

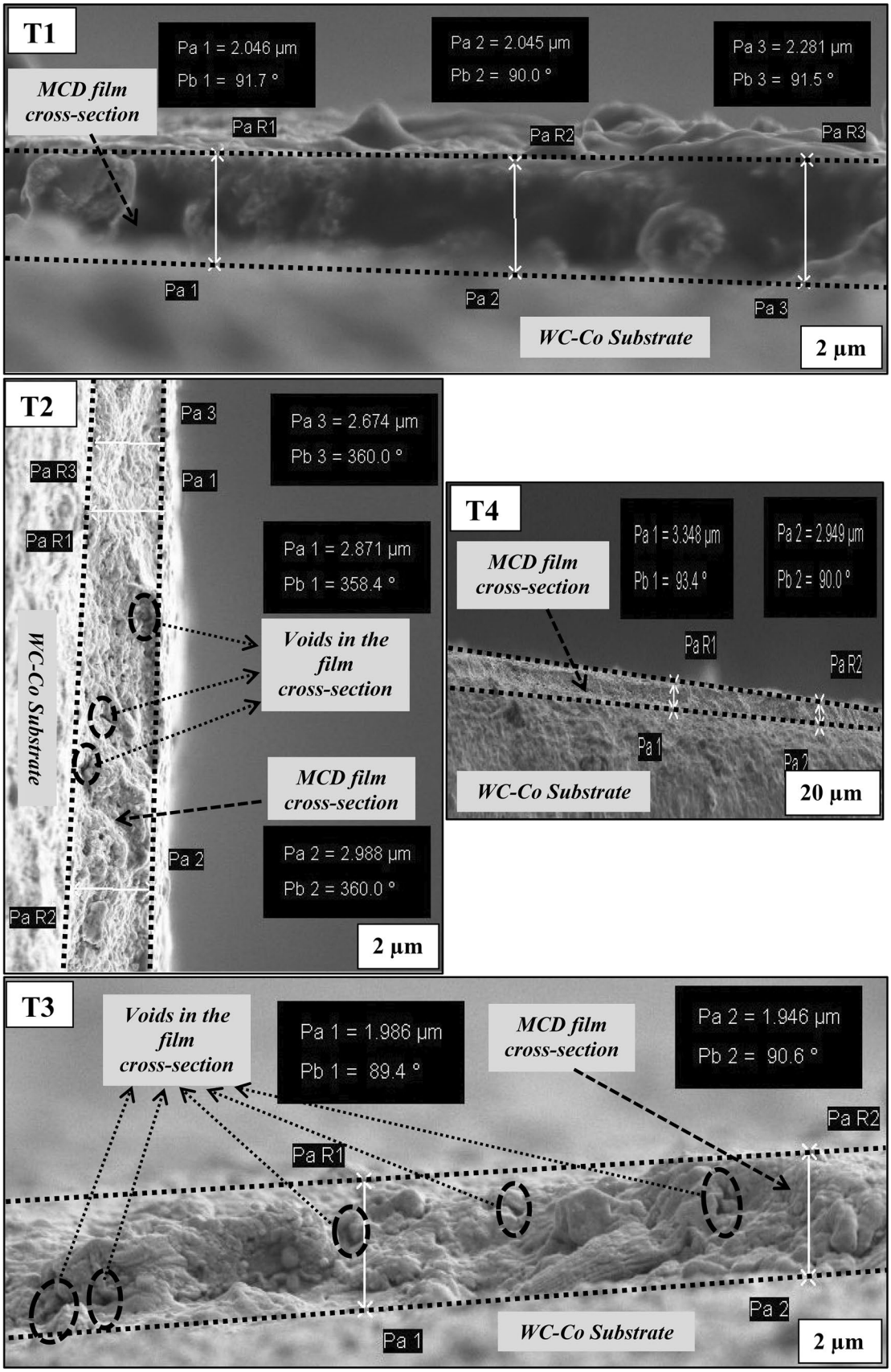

Fig. 11 FESEM cross-sectional images of the MCD film-cemented carbide substrate system for all coated samples

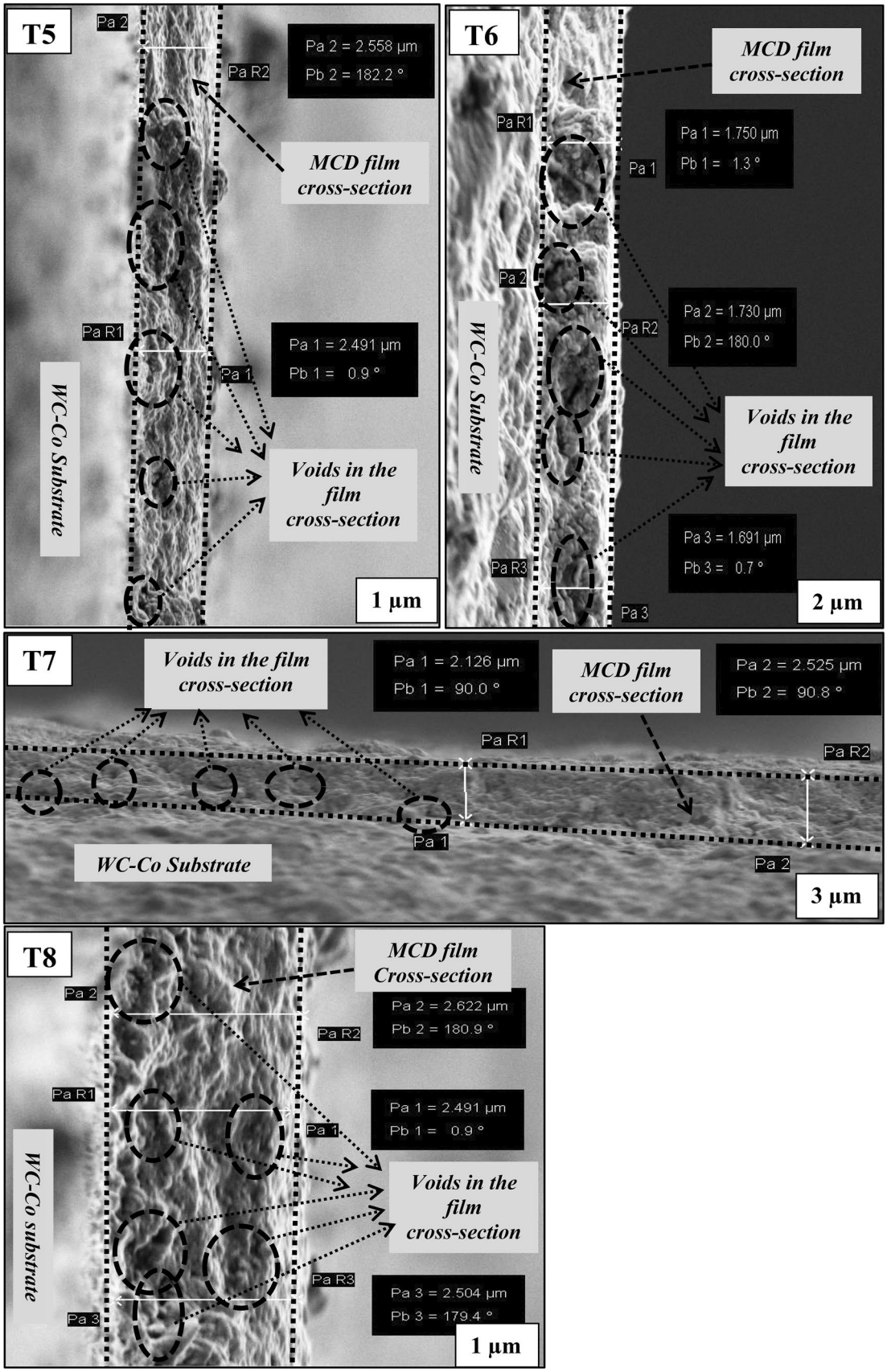

Fig. 11 (continued)

it should have better adhesive strength than the T1 sample (Raman results).

Figure 12 depicts the variable hardness (H) values ranging from (1531–1834) HV to (15–18) GPa. The variation is caused by the different percentages of carbon phases in the respective films. The higher the Csp^3–Csp^3 content, the more excellent the interfacial adhesion between the coated film and the substrate, which absorbs the shear and normal forces produced by externally applied forces [47]. The force applied by the diamond indenter caused a permanent deformation in the coated film, as shown in the figure. There is no deviation in crack propagation other than a straight line. No significant radial cracks were seen around the indentation marks, indicating a limiting plastic deformation zone with firmly adhered coatings.

Figure 13 shows the measured mean diagonal of the crack for the T4 sample is the smallest (0.0318 mm), followed by the T2 sample. Figure 12 shows the cracks in the T2, T3, and T4 films were synchronous with the cemented carbide substrate, as evidenced by no side peeling of the coating around the crack. This results in a strong interface with improved tensile strength and high ductility to withstand

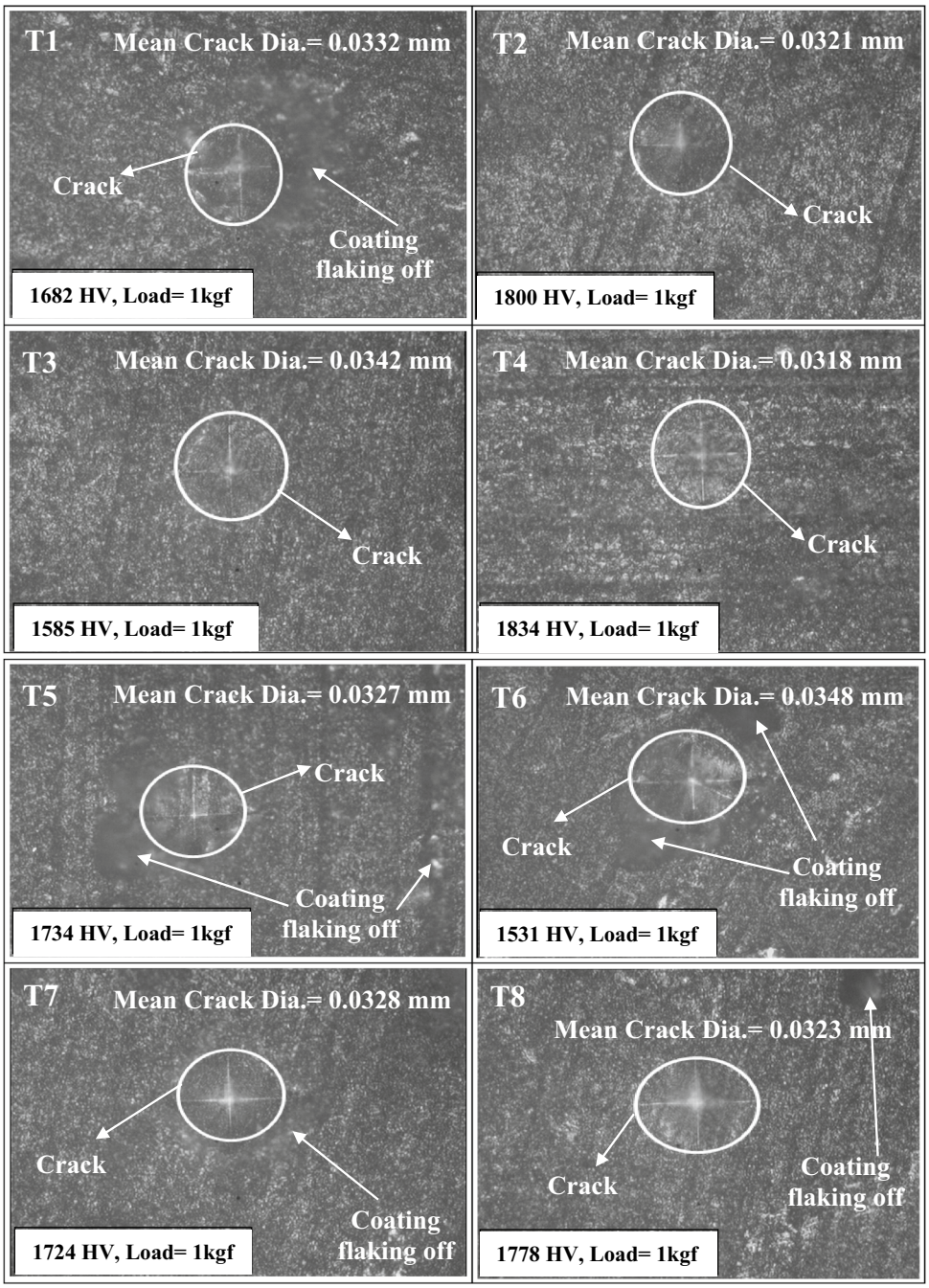

Fig. 12 Vickers microhardness results for all powders investigated for diamond coating on cemented carbide inserts

the indenter's plastic deformation force. As a result, samples T2 and T4 should have superior coating adherence and less crack propagation.

The AFM results revealed that the (T2) sample contained smaller particles (mean particle size), resulting in a more uniform distribution across the surface [48, 49]. The area of contact between the film and the substrate increased. Consequently, the indenter's impact force and crack propagation were reduced. The (T4) sample has an optimal aspect ratio; it has fewer cracks and greater adhesion strength. Table 4 shows that the (T3) sample had a large mean height of grain size with the smallest grain diameter. The narrow distribution of surface parameters like area and perimeter resulted in a larger interparticle distance. Furthermore, a very thin coating thickness with voids in the film exposes the surface to a higher direct indentation force, resulting in a larger crack diameter and a reduction in strength. Coating delamination was seen next to cracks in samples T1, T5, T6, T7, and T8, indicating that the coated film's shearing force is not synchronous with the substrate. Furthermore, the presence of voids in the film for these samples (possibly the presence of non-bonded areas at the interface) reduced the toughness at the interface. The indenter force causes crack propagation at the substrate–film interface zone, resulting in stress concentration fracture. As a result, the hardness and adhesion of these samples are reduced. Furthermore, coating delamination in these samples may be caused by high-intensity normal and residual shear stresses that exceed interfacial bonding when acted on by indentation force [50]. On the other hand, there were no voids in the (T1) sample, which had a particle size that was too small. Diamond grain aggregation (AFM results) prevented perfect bonding with WC grains at the grain boundaries.

Furthermore, the mean coating thickness for T2 and T4 samples (2.844 µm and 3.149 µm, respectively) is greater than for T1, T3, T5, T6, T7, and T8 samples (2.124 µm, 1.966 µm, 2.525 µm, 1.724 µm, 2.326 µm, and 2.539 µm, respectively). Both samples had a good coating adhesion microstructure with the shortest crack length. As a result, samples T2 and T4 have better mechanical bonding mechanisms at the interface than the other samples.

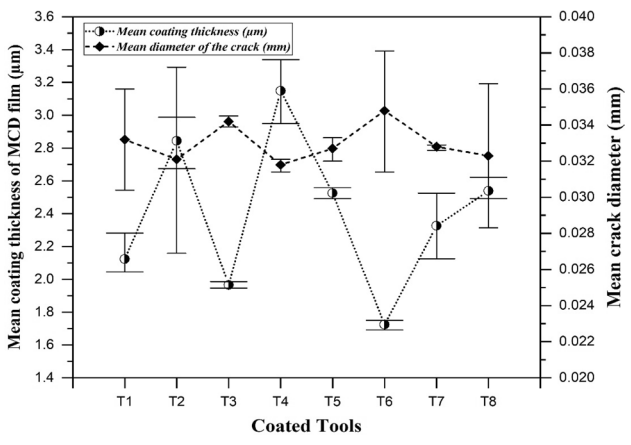

Fig. 13 Coating thickness vs. crack distribution on MCD surfaces using various seeded transitional powders (with maximum and minimum values)

As shown in Fig. 14, the MCD film separation in the T1 and T3 samples was caused by tensile residual stresses in the film. Due to the thinner film thickness in both samples, high interfacial stresses may have occurred. As a result, the combined factors of higher interfacial stress and residual stress would have resulted in greater film delamination and buckling. The T2 and T4 samples with the thickest coatings demonstrated the best resistance to coating delamination. The reason for this is that the indenter impact caused less plastic deformation of the surface, limiting the maximum crack propagation. Furthermore, both samples had more crystals per unit area (SEM images) which reduces the likelihood of void formation at the interface, and thus the possibility of coating delamination. However, micro-cracks can be seen on both the film's surfaces. The samples, T5 and T6, show cracks in both latitude and longitude directions [51]. As a result, the impact of coating delamination is expected to be greater in both samples than in other samples that show a crack only in the latitude direction. The cracks in both samples are more expansive, and their delamination is more severe. Because of the low hardness value, the film-to-substrate bonding at the interface is weak. Compared to other samples, both samples had fractures, plastic deformation, and spallation in a larger area. Samples T7 and T8 have highly compressive residual stressed films that store the maximum strain energy. The release of strain energy induced by the indenter force caused the film to delaminate [52]. The T8 sample surface has numerous holes.

Furthermore, the Raman results revealed that the samples contained a-C (samples T3, T6), a-C: H (samples T1, T2, T4, T5, T7), and ta-C: H (sample T8), but no hydrogen-free ta-C in their film. The amount of sp^3 content in the structure of films is known to be of the order: ta-C > ta-C: H > a-C: H > a-C: H > a-C, which has a direct effect on the hardness [53]. Although sample T8 had the highest sp^3 content in the film, compressive residual stresses associated with high sp^3 films (Raman findings) reduce its hardness rating [54, 55]. The polymeric a-C: H, a softer film in the T5 sample, reduced its hardness. Furthermore, the high hydrogen content of the film results in more hydrogen-bonded carbon and less sp^3-bonded carbon. As a result, the corresponding hardness values of each sample decrease, eventually resulting in film delamination. Furthermore, the coating failure in different samples was caused by differences in the crystallinity of the samples. The higher crystallinity in samples T5, T6, T7, and T8 (x-factor value from Raman results) results in more

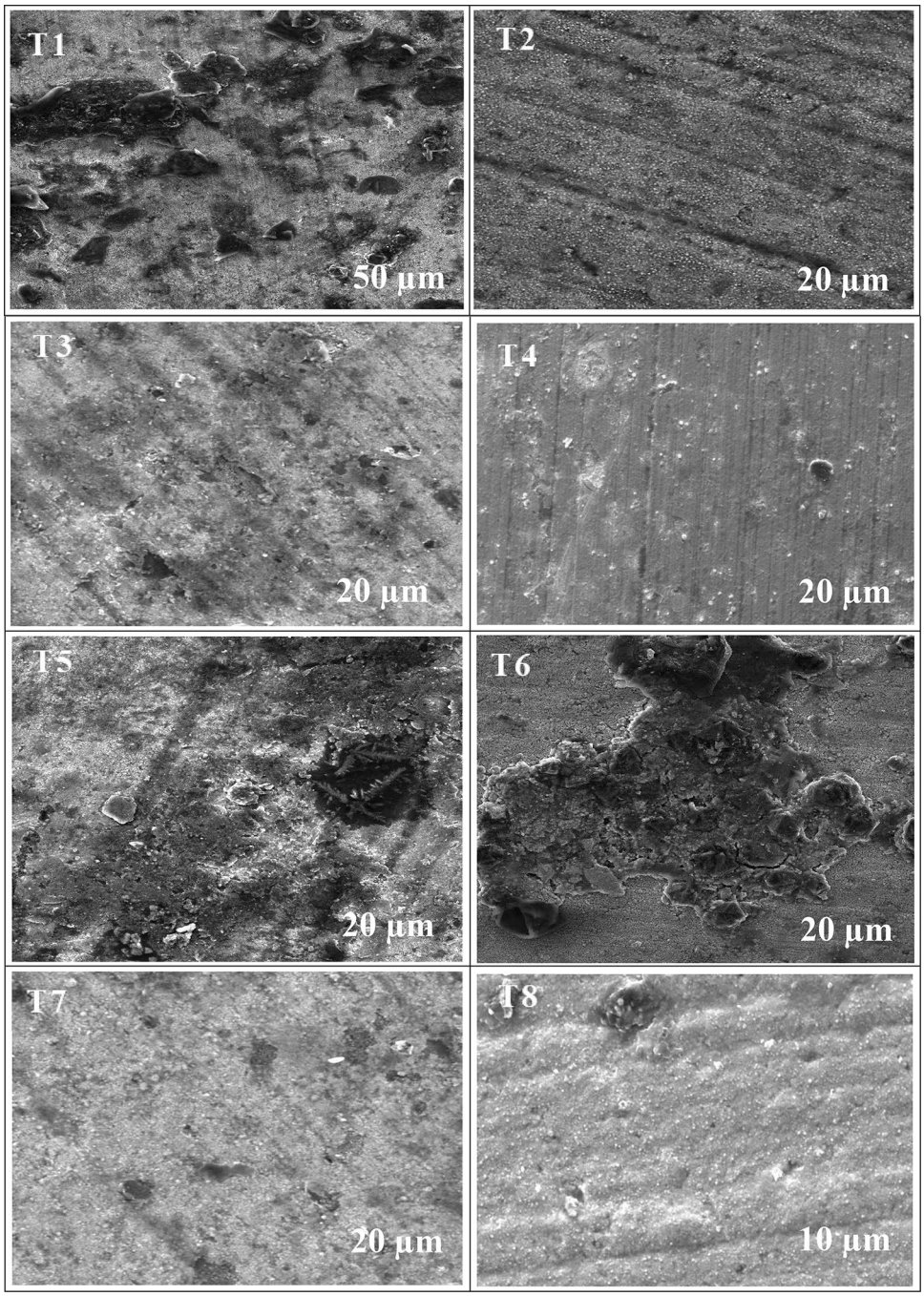

Fig. 14 SEM images of MCD film system failures after microhardness at a maximum load of 1 kgf

brittle fracture. Furthermore, a higher I_D/I_G ratio indicates that these films have lower adhesion (Table 5).

4 Conclusion

Using the HFCVD technique, the microcrystalline diamond was successfully deposited on a SPUN cemented carbide substrate. The effect of various TM powders on the properties of the deposited film was studied. The following conclusions have been reached:

1. The use of glassy carbon powders (T1) increased the rate of diamond crystal growth. Still, the crystalline quality deteriorated ($FWHM_D$) because the film contained other forms of carbon besides diamond (a higher $FWHM_G$ and I_D/I_G ratio). Despite the lack of voids at the film cross-sectional, valleys (lowest R_{ku} value) were larger in

Table 5 Comparative summary of the above results

Exp results	Samples								
	T1	T2	T3	T4	T5	T6	T7	T8	Best sample
No. of crystals	33–43	50–62	27–33	56–67	20–21	7–9	6–8	7–8	T2 and T4
Size of crystals (μm)	~2.4	~2.2	~1.2	~2.5	~2.2	~1.2	~0.8	~1.1	T1, T2, T4 and T5
$FWHM_D$ (cm^{-1})	109.22	26.13	174.41	102.38	85.15	116.4	97.49	44.50	T2
$FWHM_G$ (cm^{-1})	70.05	17.23	79.76	50.45	56.29	87.70	64.96	37.75	T2
(I_D/I_G)	1.67	1.29	2.57	1.71	5.61	5.69	3.13	3.29	T1, T2 and T4
x-factor	99.21	98.98	99.48	99.22	99.76	99.76	99.58	99.59	T1, T2, T3, and T4
Residual stress (GPa)	0.03 (+ve)	1.95 (−ve)	2.87 (+ve)	2.83 (−ve)	17.12 (−ve)	17.41 (−ve)	39.46 (−ve)	62.35 (−ve)	T2 and T4
3D peak height (nm)	< 100	~200	~300	~400	–	–	–	–	T1 and T2
R_{sk}	−0.242	0.045	−0.097	−0.53	–	–	–	–	T2
R_{ku}	1.77	2.83	2.38	2.48	–	–	–	–	T2 and T4
R_{pv} (nm)	460.36	332.77	751.24	487.63	–	–	–	–	T2
R_{max} (nm)	231.34	157.87	409.22	325.12	–	–	–	–	T2
Aspect ratio	0.12	0.09	0.22	0.16	–	–	–	–	T2
Film thickness (μm)	(2.045–2.281)	(2.674–2.988)	(1.946–1.986)	(2.949–3.348)	(2.491–2.558)	(1.691–1.750)	(2.126–2.525)	(2.491–2.622)	T2 and T4
Microhardness (HV)	1682	1800	1585	1834	1734	1531	1724	1778	T2 and T4

T1 than in T2 and T4. The film rupture was even more apparent than in other samples (Fig. 14).

2. The *x*-factor value revealed the highest nucleated MCD growth, regardless of carbide formation via tantalum powders (T2). The film had the highest crystallinity and the highest sp^3 diamond phase, and the lowest compressive residual stresses. The formation of the Ta_XC intermediate phase is expected to improve the coated tool's machining performance. The positive skewness and relatively higher kurtosis value with the lowest surface roughness (R_a, R_{rms}, and R_{max}) indicated a relatively smooth and uniform surface morphology with good grain dispersion. The microhardness value confirmed the strong adhesive strength of the coating.
3. Molybdenum powder (T3) produced a few spherical-shaped diamond crystals with no defined facets of visible MCD grains. Despite the formation of Mo_2C phases, residual stresses (tensile) in the film caused cracks at the substrate–film interface to widen, reducing the coating's adhesion strength. The AFM 3D and line profile images revealed greater height values and pits, respectively, implying that the T3 sample's performance can be negatively affected.
4. The use of diamond powder (T4) resulted in higher roughness values with larger mean grain size, comparable to the T3 sample, indicating the large size of MCD crystal growth. This sample has more peaks than in the others (line profile image). The diamond-seeded powder had the highest microhardness value, resulting in a harder coating for the sample. As a result, diamond powder with Cubo octahedral-shaped faceted crystals was thought to be better suited for the growth of a single-crystal diamond.
5. Crystals formed from palladium powder (T5) grew into diamonds of comparable size (~2.2 μm) to the T2 sample. The average sizes of diamond crystals formed versus

the seeded powder sizes used are in the following order: diamond > palladium > platinum > tungsten. The hardness value was higher due to the higher crystallinity. The cross-sectional thickness and film fracture results showed inferior adhesion in the powders.

6. The use of platinum powders (T6) resulted in very few diamond crystal nucleations and growth due to the high amorphous carbon content in the film. The mean crack length (Vickers hardness results) in the coated film was of the highest order compared to other seeded powders, with the least film thickness and adhesion.
7. The growth kinetics of diamond crystals were faster in iridium (T7) powders, which took the least amount of time to grow to the corresponding crystal size, followed by tungsten powders. These powders generated a clustered diamond with a spherical shape and a moderate adhesion strength value.
8. The use of tungsten powder (T8) resulted in moderate diamond crystal growth. The carbon availability required to grow diamonds was primarily attributed to the W_2C and WC formations. Coating delamination near cracks was observed with hardness values greater than the T7 sample.

The results demonstrate that Raman data for iridium and tungsten powders suggests substantially higher compressive residual stresses, which are undesirable. As a result, these powders can only grow diamonds and have very little mechanical application. For diamond growth, carbon, and molybdenum powders are recommended. However, due to the tensile residual stresses developed in the film, it will stretch. As a result, crack propagation is faster (as measured by microhardness) and may reach the substrate level, lowering the sample adhesion strength. Although palladium powders can be used to grow diamonds, the cauliflower-shaped crystals formed in palladium powders and the highest radial crack in platinum powders reduce both materials' tribological properties. As a result, apart from using diamond powder, the improved diamond growth in tantalum powders is valuable in our case in terms of mechanical applications.

Acknowledgements This work was supported by the AICTE-RPS-2009 (8023/BOR/RID/RPS-142/2008-09, dated 12th March 2009). The authors would like to thank all the laboratory staff of VSSUT Burla, Odisha, India for their kind support to carry out this work. We extend our heartfelt thanks to Late Mr. Minaketan Behera (Research Scholar, Mechanical Department) for his contribution to the experiments carried out. He died in January 2021 because of COVID-19. We sincerely thank Dr. Ananthakumar Ramadoss, Jr. Scientist, CIPET, Bhubaneswar, Odisha, India for his help in providing us with the AFM equipment.

Data availability The raw data required to reproduce these findings are available to download from [INSERT PERMANENT WEBLINK(s)].

The processed data required to reproduce these findings are available to download from [INSERT PERMANENT WEBLINK(s)].

Declarations

Conflict of interest The author(s) declared no potential conflicts of interest concerning the research, authorship, and/or publication of this article.

References

1. J.E. Butler, A.V. Sumant, Chem. Vap. Depos. **14**, 145–160 (2008). https://doi.org/10.1002/cvde.200700037
2. B. Trindade, M.T. Vieira, Mater. Sci. Eng. A **352**, 195–201 (2003). https://doi.org/10.1016/S0921-5093(02)00865-1
3. J.G. Buijnsters, J.P. Celis, R.W.A. Hendrikx, L. Vazquez, J. Phys. Chem. C **117**, 23322–23332 (2013). https://doi.org/10.1021/jp4071482
4. H. Itoh, T. Osaki, H. Iwahara, J. Mater. Sci. **26**, 3763–3768 (1995). https://doi.org/10.1007/BF01184968
5. Y. Chakk, R. Brener, A. Hoffman, Appl. Phys. Lett. **66**, 2819 (1995). https://doi.org/10.1063/1.113486
6. B. Baudrillart, F. Benedic, A. Tardieu, J. Achard. Phys. Status Solidi A **214**, 1700205 (2017). https://doi.org/10.1002/pssa.201700205
7. M. Varga, M. Vojs, M. Marton, L. Michalikova, M. Vesely, R. Redhammer, M. Michalka, Vacuum **86**, 681–683 (2012). https://doi.org/10.1016/j.vacuum.2011.07.035
8. S.K. Sarangi, A. Chattopadhyay, A.K. Chattopadhyay, Int. J. Refract. Metal Hard Mater. **26**, 220–231 (2008). https://doi.org/10.1016/j.ijrmhm.2007.05.002
9. S.K. Sarangi, A. Chattopadhyay, A.K. Chattopadhyay, Appl. Surf. Sci. **254**, 3721–3733 (2008). https://doi.org/10.1016/j.apsusc.2007.10.104
10. J.R. Mahajan, M.A. More, P.P. Patil, S.R. Sainkar, Mater. Sci. Eng. B **97**, 117–122 (2003). https://doi.org/10.1016/S0921-5107(02)00398-7
11. M. Vedawyas, G. Sivananthan, A. Kumar, Mater. Sci. Eng. B **78**, 16–21 (2000). https://doi.org/10.1016/S0921-5107(00)00506-7
12. F. Wang, V.N. Richards, S.P. Shields, W.E. Buhro, Chem. Mater. **26**, 5–21 (2014). https://doi.org/10.1021/cm402139r
13. D. Erdemir, A.Y. Lee, A.S. Myerson, Acc. Chem. Res. **42**, 621–629 (2009). https://doi.org/10.1021/ar800217x
14. R.T. Rozbicki, V.K. Sarin, Int. J. Refract. Metal Hard Mater. **16**, 377–388 (1998). https://doi.org/10.1016/S0263-4368(98)00055-9
15. Z. Chen, C.H. Shek, J.K.L. Lai, Physica B **358**, 56–62 (2005). https://doi.org/10.1016/j.physb.2004.12.026
16. M. Chandran, C.R. Kumaran, S. Gowthama, P. Shanmugam, R. Natarajan, S.S. Bhattacharya, M.S.R. Rao, Int. J. Refract. Metal Hard Mater. **37**, 117–120 (2013). https://doi.org/10.1016/j.ijrmhm.2012.11.005
17. S.K. Sarangi, A. Chattopadhya, A.K. Chattopadhyay, Int. J. Refract. Metal Hard Mater. **31**, 1–13 (2012). https://doi.org/10.1016/j.ijrmhm.2011.07.007
18. Y.K. Liu, Y. Tzeng, C. Liu, P. Tso, I.N. Lin, Diam. Relat. Mater. **13**, 1859–1864 (2004). https://doi.org/10.1016/j.diamond.2004.05.006
19. N. Dwivedi, S. Kumar, H.K. Malik, Mater. Chem. Phys. **137**, 7–12 (2012). https://doi.org/10.1016/j.matchemphys.2012.02.050
20. A. Erdemir, C. Donnet, J. Phys. D Appl. Phys. **39**, R311 (2006). https://doi.org/10.1088/0022-3727/39/18/R01

21. X.M. Meng, W.Z. Tang, L.F. Hei, C.M. Li, S.J. Askari, G.C. Chen, F.X. Lu, Int. J. Refract. Metal Hard Mater. **26**, 485–490 (2008). https://doi.org/10.1016/j.ijrmhm.2007.11.006
22. H.M. Soltani, M. Tayebi, Int. J. Refract. Metal Hard Mater. (2019). https://doi.org/10.1016/j.ijrmhm.2019.105172
23. E.M. Ruiz-Navas, M.L. Delgado, B. Trindade, Compos. Part A **40**, 1283–1290 (2009). https://doi.org/10.1016/j.compositesa.2009.05.022
24. M. Chandran, A. Hoffman, J. Phys. D Appl. Phys. **49**, 213002 (2016). https://doi.org/10.1088/0022-3727/49/21/213002
25. H.A. Pour, M. Lieblich, A.J. Lopez, J. Rams, M.T. Salehi, S.G. Shabestari, Compos. Part A **38**, 2536–2540 (2007). https://doi.org/10.1016/j.compositesa.2007.07.012
26. H.H. Yu, M.Y. He, J.W. Hutchinson, Acta Mater. **49**, 93–107 (2001). https://doi.org/10.1016/S1359-6454(00)00293-7
27. M. Behera, A. Jena, S.K. Pattnaik, S. Padhi, S.K. Sarangi, Mater. Chem. Phys. **256**, 123638 (2020). https://doi.org/10.1016/j.matchemphys.2020.123638
28. P.C. Redfern, D.A. Horner, L.A. Curtiss, D.M. Gruen, J. Phys. Chem. **100**, 11654–11663 (1996). https://doi.org/10.1021/jp953165g
29. L. Yang, H.Y. He, B.C. Pan, J. Chem. Phys. **138**, 24502 (2013). https://doi.org/10.1063/1.4773448
30. D.-D. Ma, Y.-P. Xue, J. Gao, Y. Ma, S.-W. Yu, Y.-S. Wang, C. Xue, H.-J. Hei, B. Tang, Appl. Surf. Sci. **527**, 146727 (2020). https://doi.org/10.1016/j.apsusc.2020.146727
31. F.E. Palomar, P.C. Zambrano, M.I. Gomez, R. Colas, M.P. Guerrero, A. Castillo, Vacuum **84**, 1236–1239 (2010). https://doi.org/10.1016/j.vacuum.2009.10.032
32. J.G. Buijnsters, L. Vazquez, G.W.G. van-Dreumel, J.J.T. Mulen, W.J.P.V. Enckevort, J. Appl. Phys. **108**, 103514–103522 (2010). https://doi.org/10.1063/1.3506525
33. V.J. Trava-Airoldi, E.J. Corat, L.V. Santos, A.V. Diniz, J.R. Moro, N.F. Leite, Diam. Relat. Mater. **11**, 532–535 (2002). https://doi.org/10.1016/S0925-9635(01)00721-X
34. M. Roy, K. Mali, N. Joshi, D.S. Misra, S.K. Kulshreshtha, Diam. Relat. Mater. **16**, 517–525 (2007). https://doi.org/10.1016/j.diamond.2006.10.002
35. W. Kalss, R. Haubner, G. Lippold, B. Lux, Diam. Relat. Mater. **7**, 158–164 (1998). https://doi.org/10.1016/S0925-9635(97)00209-4
36. M.J. Verstraete, J.C. Charlier, Appl. Phys. Lett. **86**, 191917–191919 (2005). https://doi.org/10.1063/1.1922571
37. T. Bai, Y. Wang, T. Feygelson, M.J. Tadjer, K.D. Hobart, N.J. Hines, L. Yates, S. Graham, J. Anaya, M. Kuball, J. Solid State Sci. Technol. **9**, 053002 (2020). https://doi.org/10.1149/2162-8777/ab96d8
38. A. Paritosh, D.J. Srolovitz, C.C. Battaile, X. Li, J.E. Butler, Acta Mater. **47**, 2269–2281 (1999). https://doi.org/10.1016/S1359-6454(99)00086-5
39. T. Guillemet, Z.Q. Xie, Y.S. Zhou, J.B. Park, A. Veillere, W. Xiong, J.M. Heintz, J.F. Silvain, N. Chandra, Y.F. Lu, A.C.S. Appl, Mater. Interfaces **3**, 4120–4125 (2011). https://doi.org/10.1021/am201010h
40. K. Fabisiak, R.T. Piotrowska, E. Staryga, M. Szybowicz, K. Paprocki, A. Banaszak, P. Popielarski, Mater. Sci. Eng. B **177**, 1352–1357 (2012). https://doi.org/10.1016/j.mseb.2011.12.013
41. H. Ejalonibu, G. Sarty, M. Bradley, Mater. Sci. Eng. B **258**, 114559 (2020). https://doi.org/10.1016/j.mseb.2020.114559
42. G.A. Abbas, S.S. Roy, P. Papakonstantinou, J.A. McLaughlin, Carbon **43**, 303–309 (2005). https://doi.org/10.1016/j.carbon.2004.09.016
43. T.S. Santra, C.H. Liu, T.K. Bhattacharyya, P. Patel, T.K. Barik, J. Appl. Phys. **107**, 124320 (2010). https://doi.org/10.1063/1.3415548
44. A. Glaser, H.G. Jentsch, S.M. Rosiwal, A. Ludtke, R.F. Singer, Mater. Sci. Eng. B **127**, 186–192 (2006). https://doi.org/10.1016/j.mseb.2005.10.018
45. T. Liu, D. Raabe, W. Mao, S. Zaefferer, Adv. Funct. Mater. **19**, 3880–3891 (2009). https://doi.org/10.1002/adfm.200901231
46. S. Zhang, X. Zhang, Thin Solid Films **520**, 2375–2389 (2012). https://doi.org/10.1016/j.tsf.2011.09.036
47. P. Hess, J. Appl. Phys. **111**, 051101 (2012). https://doi.org/10.1063/1.3683544
48. B. Xu, Y. Tian, J. Phys. Chem. C **119**, 5633–5638 (2015). https://doi.org/10.1021/acs.jpcc.5b00017
49. Y.L. Godec, A. Courac, V.L. Solozhenko, J. Appl. Phys. **126**, 151102 (2019). https://doi.org/10.1063/1.5111321
50. R. Ikeda, M. Hayashi, A. Yonezu, T. Ogawa, M. Takemoto, Diam. Relat. Mater. **13**, 2024–2030 (2004). https://doi.org/10.1016/j.diamond.2004.08.003
51. A.A. Vereschaka, S.N. Grigoriev, Wear **378–379**, 43–57 (2017). https://doi.org/10.1016/j.wear.2017.01.101
52. S. Sekhar, V. Kandula, in *Laser Technology: Applications in Adhesion and Related Areas* (2018), p. 269–298. https://doi.org/10.1002/9781119185031.ch7
53. K.A.H. Al Mahmud, M.A. Kalam, H.H. Masjuki, H.M. Mobarak, N.W.M. Zulkifli, Crit. Rev. Solid State Mater. Sci. **40**, 90–118 (2014). https://doi.org/10.1080/10408436.2014.940441
54. L.Y. Huang, J. Lu, K.W. Xu, Mater. Sci. Eng. A **373**, 45–53 (2004). https://doi.org/10.1016/j.msea.2003.12.032
55. X. Sui, X. Wang, S. Zhang, M. Yan, W. Li, J. Hao, W. Liu, Adv. Mater. Interfaces **7**, 2000857 (2020). https://doi.org/10.1002/admi.202000857